

Supporting Information for

Seamless Staircase Electrical Contact to Semiconducting Graphene Nanoribbon

Chuanxu Ma,[†] Liangbo Liang,^{*,†} Zhongcan Xiao,[‡] Alexander A. Puretzky,[†] Kunlun Hong,[†]
Wenchang Lu,^{†,‡} Vincent Meunier,[§] J. Bernholc,^{†,‡} and An-Ping Li^{*,†}

[†]Center for Nanophase Materials Sciences, Oak Ridge National Laboratory, Oak Ridge, Tennessee
37831, United States

[‡]Department of Physics, North Carolina State University, Raleigh, North Carolina 27695, United
States

[§]Department of Physics, Applied Physics, and Astronomy, Rensselaer Polytechnic Institute, Troy,
New York 12180, United States

*Email: apli@ornl.gov; liangl1@ornl.gov

DFT simulations of the width-dependent vibration modes in aGNRs

For both BLM and SLM modes, our calculations in Figure S5 suggest a linear dependence of their frequencies on the inverse of the square root of the GNR width, $\omega = a \frac{1}{\sqrt{W}} + b$, where a and b are the fitting constants, and W is the GNR width defined as the distance between the outmost carbons in the direction perpendicular to the nanoribbon axis. Such linear dependence has been previously reported for the BLM (ref. 28). Here $W = (N - 1)\sqrt{3}L/2$, where N is the number of carbons and $L = 1.42 \text{ \AA}$ is the C-C bond length. Therefore, we have $\omega = a \frac{1}{\sqrt{1.229756(N-1)}} + b$. Based on DFT-computed frequencies of the BLM and SLM in the 7, 9, and 14-aGNRs (Supplementary Table 1 below), we can obtain the fitting constants $a = 1658.5 \text{ cm}^{-1} \text{ \AA}^{1/2}$ and $b = -209.4 \text{ cm}^{-1}$ for the BLM, and $a = 1098.9 \text{ cm}^{-1} \text{ \AA}^{1/2}$ and $b = -143.6 \text{ cm}^{-1}$ for the SLM. Based on the available experimental frequencies of the BLM in the 7, 9, and 14-aGNRs from this work and the literature (refs 12, 26), the fitting constants are $a = 1667.4 \text{ cm}^{-1} \text{ \AA}^{1/2}$ and $b = -218.5 \text{ cm}^{-1}$ for the BLM. Note that the LDA approximation used in DFT systematically overestimates the frequencies of the BLM by $\sim 6 \text{ cm}^{-1}$, compared to the experimental values.

Staircase corner induced LDOS enhancements

In Figure S8, there is no Gaussian broadening of the position and energy for the calculated LDOS map. The interface corner is on the bottom edges, and thus the LDOS map here can directly probe the interface corner. For the 7-aGNR segment, its HOMO is located around -0.8 eV, while the LUMO is around 0.9 eV, so its bandgap is ~ 1.7 eV. Interestingly, its HOMO and LUMO states extend to the 14-aGNR segment, although the signals in the 14-aGNR segment are weaker. This is partly attributed to the seamless structure characteristics of the HJ with the same sp^2 carbon-carbon bonds across the entire system. Within the ~ 1.7 eV bandgap of the 7-aGNR, multiple states from the 14-aGNR can be observed, including the HOMO located around -0.1 eV and the LUMO around 0.1 eV. Notably, many of them exhibit stronger signals around the interface than in the interior of the 14-aGNR. In addition, they can also spread into the 7-aGNR segment. For the states near the HOMO or LUMO of the 7-aGNR, orbital hybridization can occur and their spreading into the 7-aGNR is more extensive than that of the HOMO and LUMO of the 14-aGNR, which are far away from the HOMO or LUMO of the 7-aGNR.

In Figure S9, the LDOS mapping does not directly probe the interface corner. Consequently, different from the Figure 3c,d, there is no noticeable LDOS enhancement at the junction, suggesting that the enhanced LDOS observed in the Figure 3 is largely from the interface corner. On the other side, the States 4 and 5 show clearly LDOSs in the bulk of the 14-aGNR, indicating that they are not completely localized at the interface corner.

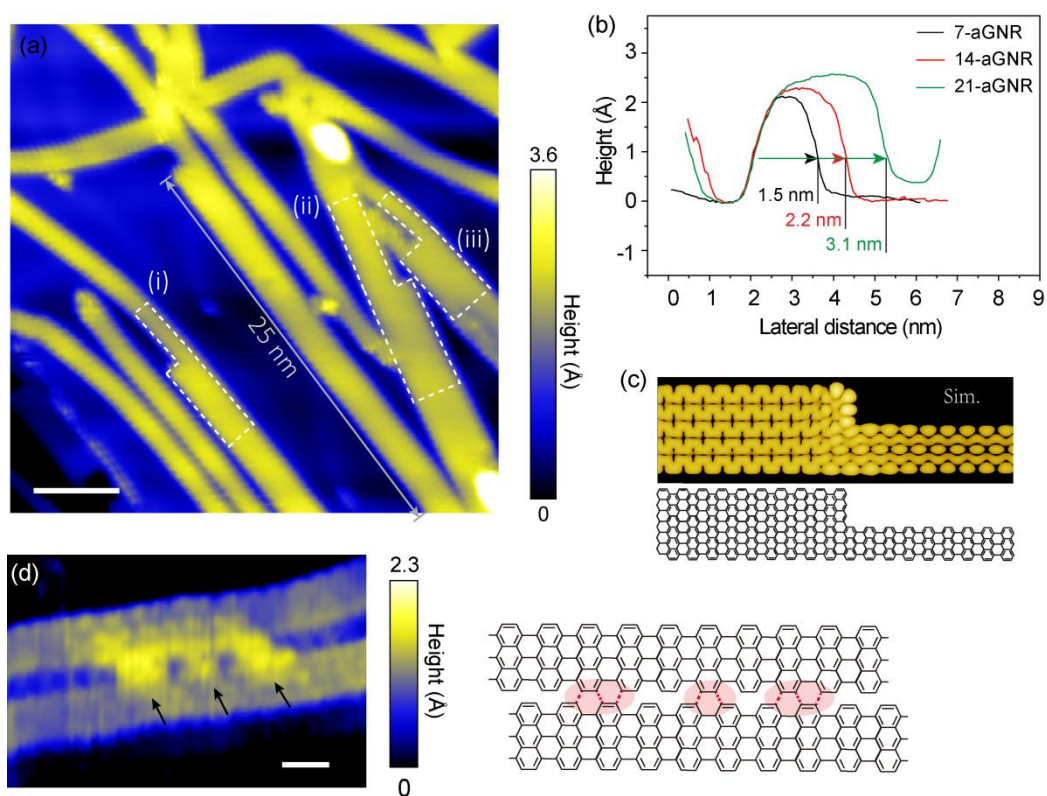


Figure S1. Formation of armchair graphene nanoribbons (aGNRs) with different widths and the heterojunctions (HJs). (a) Large-area scanning tunneling microscopy (STM) image showing the formation of aGNRs with widths of seven, fourteen and twenty-one carbon (7, 14, and 21-aGNRs) and junctions by fusing GNRs together, after 770 K annealing (sample voltage $V_s = -1.0$ V, tunneling current $I_t = 100$ pA). Three different HJs are marked: (i) the 7–14, (ii) 14–21, and (iii) 7–21 aGNR HJs. One of the 14-aGNRs showing a length more than 25 nm also is marked. Scale bar, 5 nm. (b) Profiles showing the apparent widths of the 7, 14, and 21-aGNR as 1.5 nm, 2.2 nm, and 3.1 nm, respectively. (c) Simulated STM image of the 7–14 aGNR HJ together with the atomic structure. (d) STM image showing two parallel 7-aGNRs starting to conjugate at the sites marked with black arrows, schematically illustrated by an atomic structure. Scale bar, 1 nm.

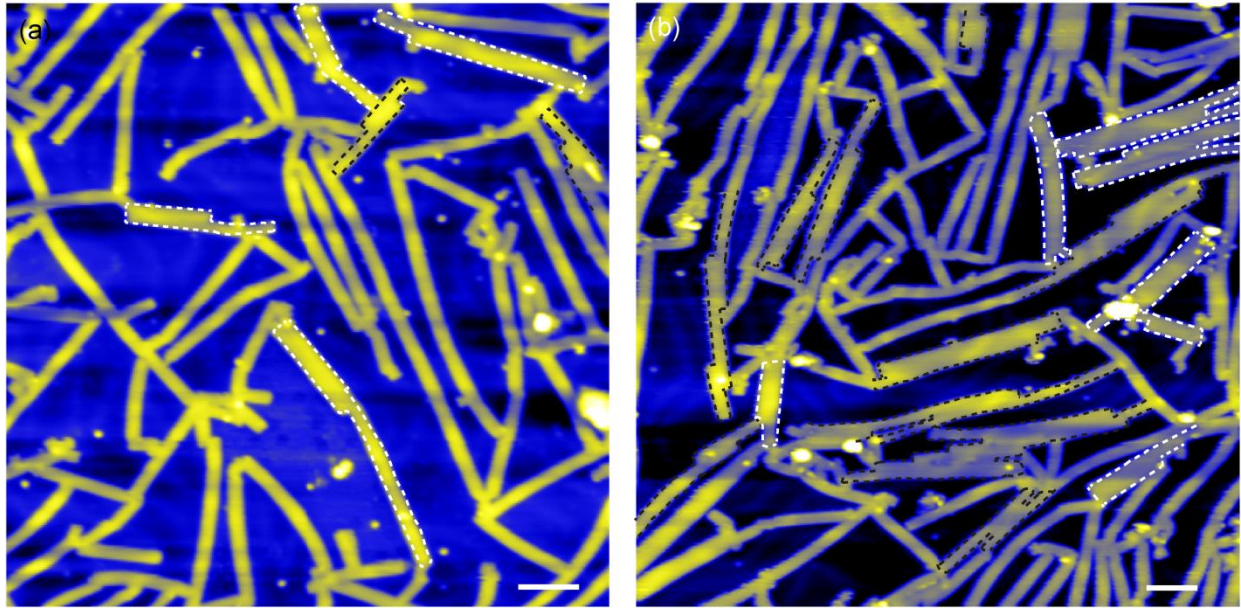


Figure S2. Large-area STM images of GNRs with different nanoribbon coverages after 770 K annealing. (a) $50 \times 50 \text{ nm}^2$, coverage of 0.2 monolayer. (b) $60 \times 60 \text{ nm}^2$, coverage of 0.6 monolayer. Setpoint for both images: $V_s = -2 \text{ V}$, $I_t = 100 \text{ pA}$. All scale bars, 5 nm. The averaged fusion ratio between the fused 7-aGNRs to the total number of ribbons is about 18% at 0.2 monolayer coverage, and about 45% at 0.6 monolayer coverage. The ratios of the newly formed 14-aGNRs and 21-aGNRs in the total number of ribbons at 0.2 monolayer coverage are about 10% and 1.5%, respectively, and about 16% and 6%, respectively, at 0.6 monolayer coverage. The white and black dashed lines mark the heterojunction edges with the wider GNRs at the ends and other locations, respectively, which show a ratio of about 1:1. Only the heterojunctions conjugated side-by-side are considered here.

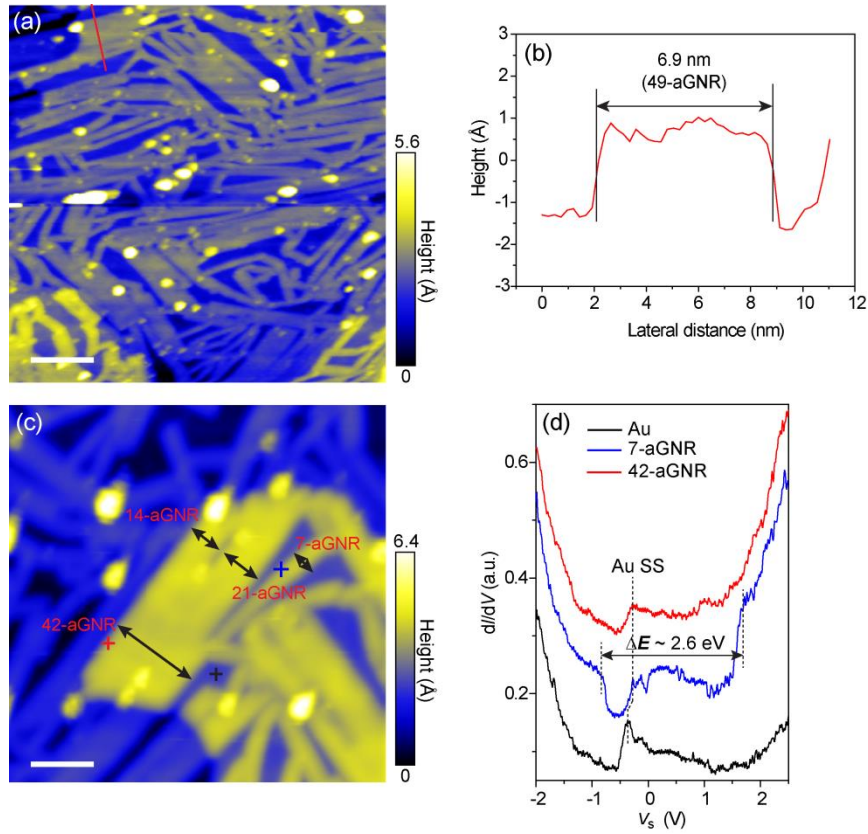


Figure S3. Formation of flake-like wide GNRs. (a) Large-area STM image of GNRs after 870 K annealing, where wide flake-like graphene are formed ($V_s = -2$ V, $I_t = 30$ pA). Scale bar, 10 nm. (b) Profile along the red line in panel a, showing a wide GNR with a width of about 6.9 nm of a 49-aGNR. (c) STM image showing the formation of a wide 42-aGNR ($V_s = -2$ V, $I_t = 20$ pA). Scale bar, 5 nm. (d) dI/dV curves taken at the cross-marked sites in panel c ($V_s = -2$ V, $I_t = 100$ pA). Black curve: Reference spectrum acquired at the bare Au(111) region (marked with a black cross) shows clear Au(111) surface state (Au SS) at about -0.4 eV. Blue curve: Spectrum acquired at the 7-aGNR edge (marked with a blue cross) shows a typical bandgap of about 2.6 eV. Red curve: Spectrum acquired at the 42-aGNR edge (marked with a red cross) shows no bandgap. Similarly to Figure 3 and 4, upshifted Au SS at the GNR regions is also observed here. The spectra are equally vertically shifted for clarity.

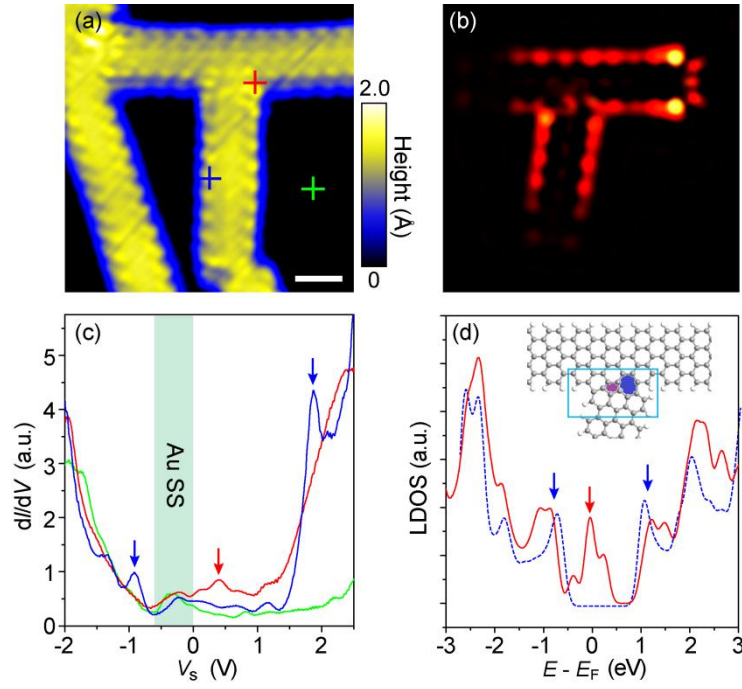


Figure S4. Structural and electronic properties of the 7–7 aGNR T-junctions formed by two nearly perpendicular GNRs. (a) High-resolution STM image showing a 7–7 aGNR T-junction. Scale bar, 1 nm. (b) Simulated STM image of the T-junction. (c) dI/dV curves acquired at the marked sites in panel a ($V_s = -2.0$ V, $I_t = 200$ pA). The shaded region marks the Au SS, blue arrows mark the highest occupied molecular orbital (HOMO) and the lowest unoccupied molecular orbital (LUMO) of the 7-aGNR, and the red arrow marks the localized states at the junction. (d) Simulated local densities of states (LDOS) of the 7-aGNR bulk (black dashed curve) and the junction region (red solid curve), respectively. Inset: The atomic structure of the T-junction with a pair of the pentagon and heptagon.

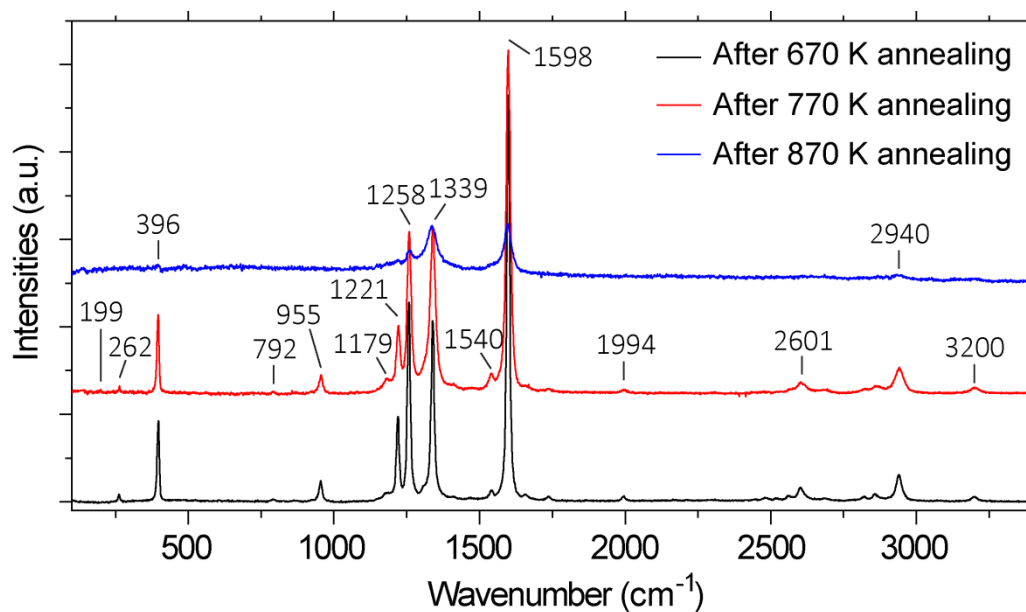


Figure S5. Raman spectra of the densely packed GNRs annealed at different temperatures. The spectra are obtained by subtracting the background of Au, after 670 K (black), 770 K (red), and 870 K (blue) annealing, respectively.

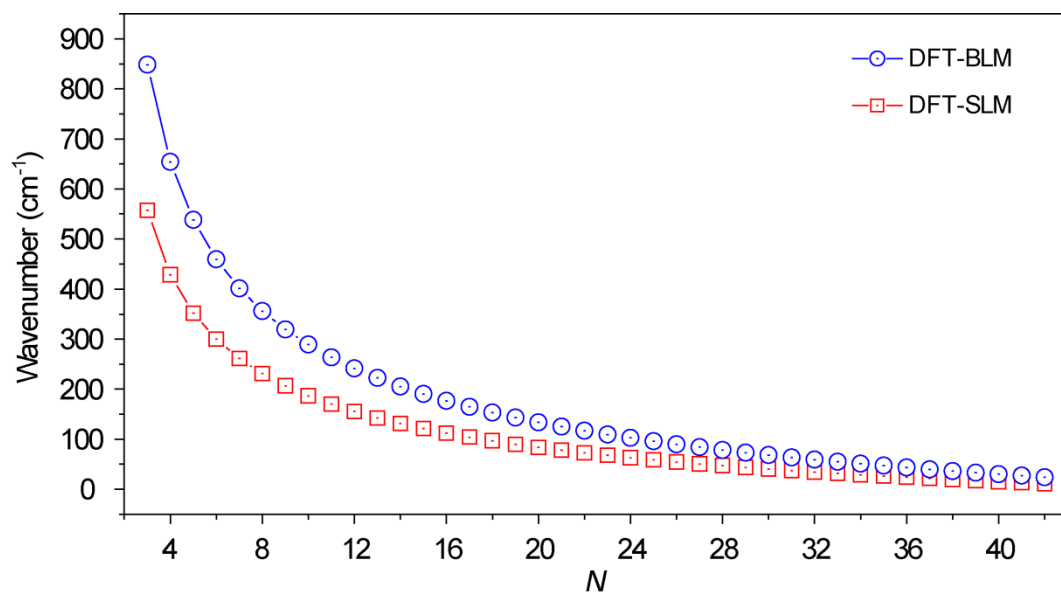


Figure S6. Density functional theory (DFT)-predicted frequencies of the width-dependent breathing-like mode (BLM) and shear-like modes (SLM) in the aGNRs.

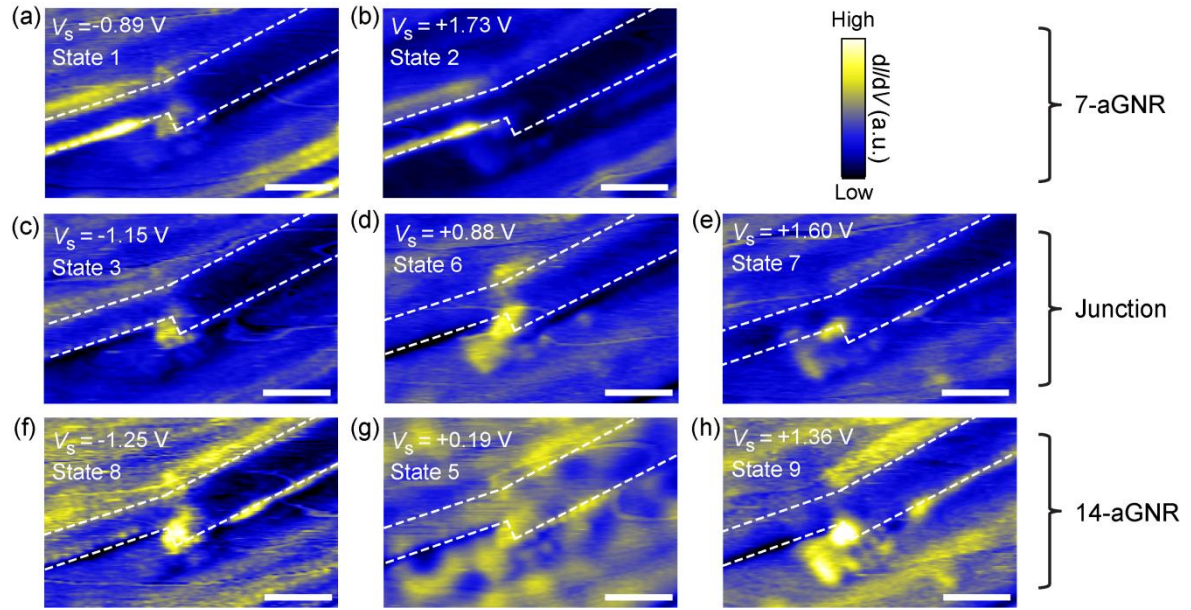


Figure S7. Experimental dI/dV spatial maps of the 7–14 aGNR HJ. The maps are recorded at the energies, marked in each image, of the States 1–3 and 5–9, same as in Figure 3b. (a–b) States 1 and 2 in the 7-aGNR. (c–e) States 3, 6, and 7 at the HJ interface. (f–h) States 5, 8, and 9 in the 14-aGNR. Dashed lines are drawn at the edge positions of the 7–14 aGNR HJ. Setpoint: $I_t = 100$ pA. All scale bars, 2 nm.

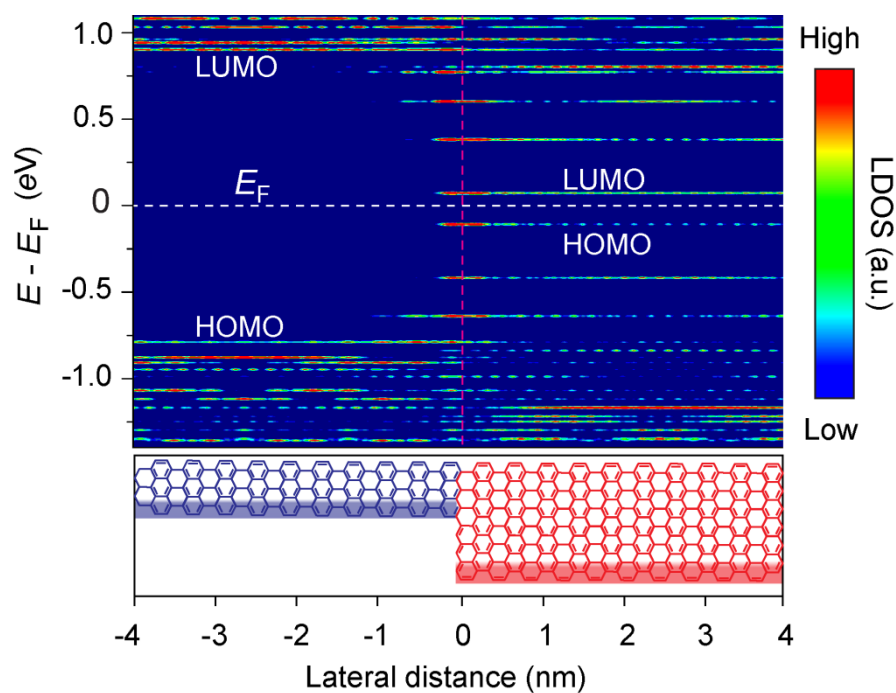


Figure S8. Simulated LDOS map across the 7–14 aGNR HJ along the staircase edges. The atomic structure shows the staircase edges marked with shadow regions. The HOMOs and LUMOs in the 7-aGNR and the 14-aGNR are marked, while the white dashed line indicates the Fermi level (E_F). The pink dashed line marks the junction.

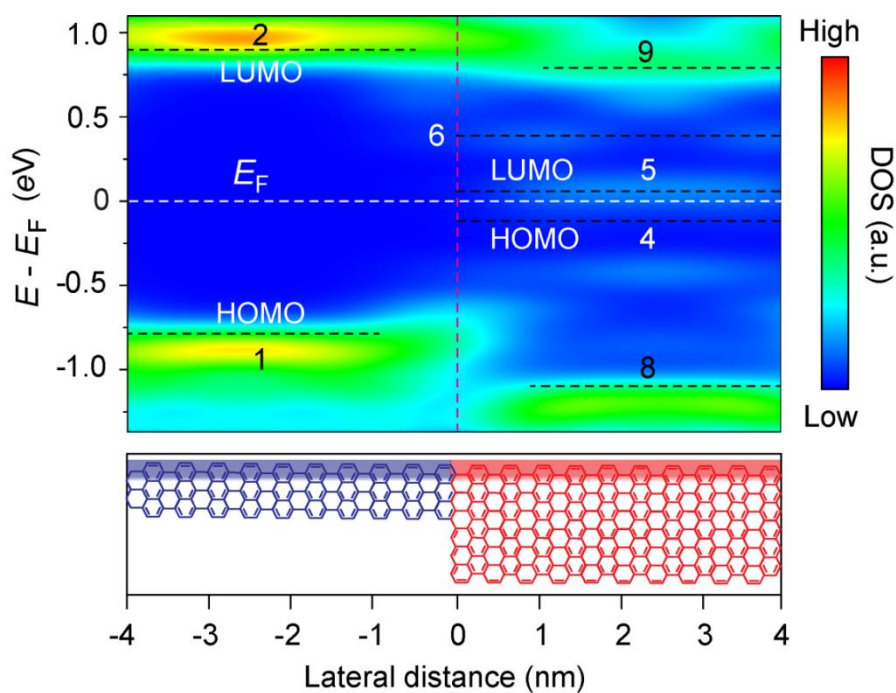


Figure S9. The simulated LDOS map across the 7–14 aGNR HJ along the straight edge. The atomic structure shows the straight edge marked with shadow regions. The HOMO and LUMO in the 7-aGNR and states in the 14-aGNR are labeled and marked with black dashed lines, while the white dashed line indicates the E_F . The pink dashed line marks the junction.

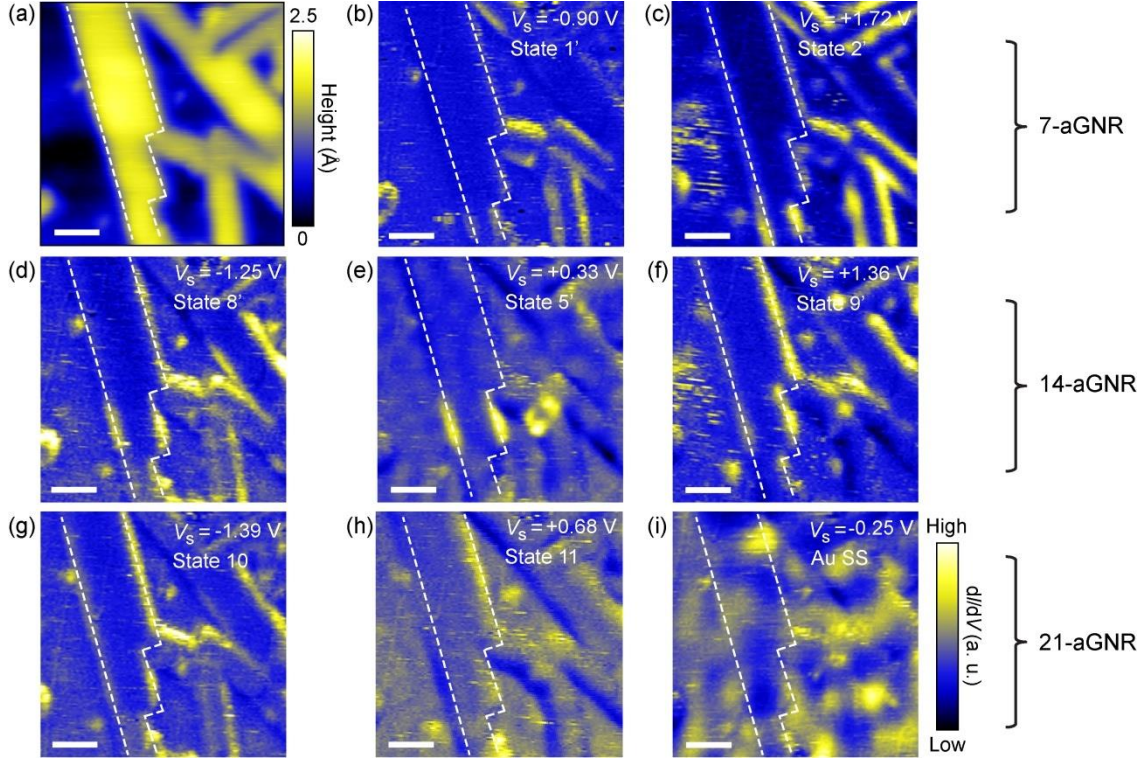


Figure S10. Experimental dI/dV spatial maps of the 7–14–21 aGNR HJ. The maps are recorded at the energies of states, marked in each image, same as the one in Figure 4b. (a) STM image recorded to measure the series of dI/dV spectra ($V_s = -2.0$ V, $I_t = 100$ pA). (b–c) States 1' and 2' in the 7-aGNR. (d–f) States 5', 8', and 9' in the 14-aGNR. (g–h) States 10 and 11 in the 21-aGNR. (i) dI/dV spatial map recorded at -0.25 V (Au SS). Dashed lines are drawn at the edge positions of the 7–14–21 aGNR HJ. Setpoint: $I_t = 100$ pA. All scale bars, 2 nm. The State 5/5' in the 14-aGNR segment shows a clear feature of the quantum dot confined between the 7 and 21-aGNRs.

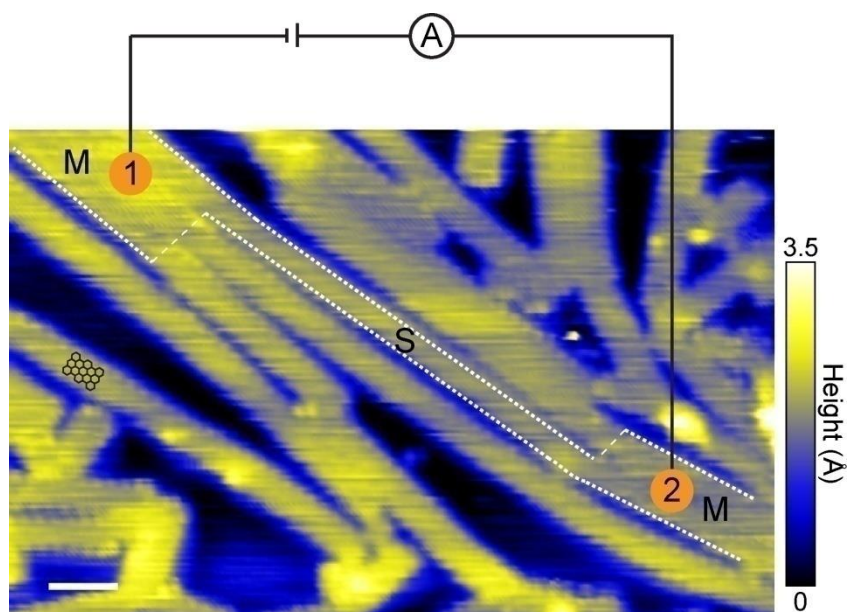


Figure S11. Proposed GNR heterojunction device. STM image was acquired at $V_s = -0.5$ V, $I_t = 200$ pA. The 21-aGNR (labeled as 1) and 14-aGNR (labeled as 2) are used as electrical contacts to the semiconducting channel material 7-aGNR. This HJ device should have lower Schottky barriers than those obtained by direct deposition of conventional metal contacts on a narrow 7-aGNR. Scale bar, 2 nm.

Table S1. DFT-calculated frequencies of the breathing-like mode (BLM) and the shear-like mode (SLM) in the 7, 9, and 14-aGNRs , with the corresponding available experimental values. “-” indicates the experimental data not available.

| Width | BLM (cm ⁻¹) | | SLM (cm ⁻¹) | |
|---------|-------------------------|--------------------|-------------------------|------------------|
| | theory | experiment | theory | experiment |
| 7-aGNR | 402 | 396 ^{a,b} | 262 | 262 ^a |
| 9-aGNR | 318 | 312 ^c | 205 | - |
| 14-aGNR | 206 | 199 ^a | 132 | - |

^a experimental data from this work.

^b experimental data from Ref. 12.

^c experimental data from Ref. 26.